



**HAL**  
open science

## Crustal accretion at a sedimented spreading center in the Andaman Sea

Aurélie Jourdain, Satish Singh, Javier Escartin, Yann Klinger, K.A. Kamesh Raju, J. Mcardle

► **To cite this version:**

Aurélie Jourdain, Satish Singh, Javier Escartin, Yann Klinger, K.A. Kamesh Raju, et al.. Crustal accretion at a sedimented spreading center in the Andaman Sea. *Geology*, 2016, 44 (5), pp.351-354. 10.1130/G37537.1 . hal-02330296

**HAL Id: hal-02330296**

**<https://hal.science/hal-02330296>**

Submitted on 19 Oct 2021

**HAL** is a multi-disciplinary open access archive for the deposit and dissemination of scientific research documents, whether they are published or not. The documents may come from teaching and research institutions in France or abroad, or from public or private research centers.

L'archive ouverte pluridisciplinaire **HAL**, est destinée au dépôt et à la diffusion de documents scientifiques de niveau recherche, publiés ou non, émanant des établissements d'enseignement et de recherche français ou étrangers, des laboratoires publics ou privés.

1 Crustal accretion at a sedimented spreading center in the  
2 Andaman Sea

3 Aurélie Jourdain<sup>1</sup>, Satish C. Singh<sup>1</sup>, Javier Escartin<sup>1</sup>, Yann Klinger<sup>1</sup>, K. A. Kamesh Raju<sup>2</sup>,  
4 J. McArdle<sup>3</sup>

5 *<sup>1</sup>Institut de Physique du Globe de Paris, Sorbonne Paris Cité, UMR7154-CNRS, 1 rue Jussieu,*  
6 *78238 Paris Cedex 05, France*

7 *<sup>2</sup>CSIR-National Institute of Oceanography, Dona Paula, Goa 403 004, India*

8 *<sup>3</sup>Petroleum Geo-services, 111 Somerset Road, Singapore 238164*

9

10 **ABSTRACT**

11 The combination of magmatic, tectonic, and hydrothermal processes that from the  
12 oceanic crust, relatively well understood along mid-ocean spreading centers, is strongly modified  
13 at sedimented spreading centers, which are still poorly understood owing to the lack of good  
14 crustal images. Here we present high-resolution deep seismic reflection images across the  
15 sedimented slow-spreading Andaman Sea spreading center that shows several sub-horizontal  
16 sills injected within the sedimentary strata beneath the axial graben. Below this sill-sediment  
17 sequence we observe reverse polarity reflections within the igneous crust, indicative of the  
18 existence of axial magma lenses (AMLs) at different depths. This results in a heterogeneous  
19 upper crust that incorporates metamorphosed sediments. The faults within the axial valley are  
20 steeply dipping (65-75°) and are in a stair-cased pattern. Their base coincides with a shallow  
21 dipping (30°) reflection, possibly defining the spreading axis morphology, controlled by the  
22 AMLs. We propose that as the sill-sediment sequences move away from the axial graben, they

23 are rotated and buried due to subsidence and faulting, forming the upper oceanic crust. The  
24 Moho reflections are observed along a significant part of the profiles, allowing the  
25 characterization of the whole crustal structure. We find that the upper oceanic crust is formed by  
26 a combination of sill-sediment sequence, followed by a thick gabbroic lower crust with some  
27 sediment along faults, with a mantle transition containing dunite lenses near the Moho.

28

## 29 **INTRODUCTION AND SETTING**

30

31 The oceanic crust forms at mid-ocean spreading centers by a combination of magmatic, tectonic,  
32 and hydrothermal processes that are relatively well studied along both fast- and slow-spreading  
33 mid-ocean ridges. However, sediments can drown spreading centers in the vicinity of continents  
34 or during the early stages of continental rifting and oceanization, as observed in the Guaymas  
35 Basin (Lizarralde et al., 2011; Kluesner et al, 2014), northern Juan de Fuca Ridge (Davis and  
36 Becker 2002), and Mohns Ridge (Bruvoll et al., 2009). These sediments capping spreading  
37 centers can significantly modify the axial thermal regime and fluid circulation, and therefore the  
38 accretion processes (melt emplacement, faulting), and also the overall lithospheric structure and  
39 composition. To better understand the impact of sedimentation on crustal accretion, we present  
40 the first whole-crust, high-resolution multichannel seismic reflection images across the  
41 sedimented Andaman Sea Spreading Center (ASSC). The unprecedented resolution of these data  
42 allow us to image clearly the interactions of sedimentation and accretion, and to propose a  
43 general model of lithospheric formation and whole-crust structure at sedimented mid-ocean  
44 ridges.

45

46 The ASSC back-arc spreading center separates the Burmese sliver plate to the northwest from  
47 the Sunda plate (Eurasia) to the southwest (Fig. 1A) (Curry et al., 1979; Kamesh Raju et al.,  
48 2004). It connects the northern Sagaing strike-slip fault with the southern Andaman-Nicobar and  
49 Sumatra faults (Sieh and Natawidjaja, 2000), which result from strain partitioning from the  
50 oblique Indian plate subduction beneath the Sunda plate (Fitch, 1972). Based on magnetic  
51 anomalies on the westernmost non-sedimented segment, ASSC spreading initiated 4 Ma ago at a  
52 full rate of 16 mm/yr, speeding to 38 mm/yr 2 Ma ago (Kamesh Raju et al., 2004).

53  
54 Most of the Andaman Sea basin is sedimented and flat lying at 3000 m water depth. The ASSC,  
55 at the center of the basin, displays a ~12 km wide axial valley, and an also flat-lying rift valley  
56 floor at 3600 m water depth (Fig. 1B), infilled by sediments from the Irrawaddy river basin in  
57 Myanmar (Fig. 1A) (Curry et al., 1979). This sedimented axial graben is bound by normal faults  
58 and tilted fault blocks, reminiscent of the structure found at slow spreading ridges (e.g.,  
59 Needham and Francheteau, 1974).

60

## 61 **SEISMIC DATA**

62

63 The seismic reflection data were acquired by Petroleum Geo-Services (PGS) in 2008 with a 6400  
64 cubic inch air gun array and recorded by an 8-km long streamer with a group spacing of 12.5 m.  
65 The air gun and the streamer were towed at 8 m and 10 m below the sea surface respectively,  
66 with a 25 m shot interval and a 9 s record length. Data were processed using a conventional time  
67 migration technique, which includes swell noise removal, trace editing to remove noisy traces,  
68 common midpoint binning, velocity analysis, upper mute, and stacking. Stacked data were

69 migrated using a post-stack Kirchhoff migration technique. PGS provided the final migrated data  
70 and root mean square (RMS) velocities every 1 km (160 CMP), and no pre-stack data were  
71 available for our study. Here we present two N-S profiles crossing the sedimented segment of the  
72 ASSC and spaced ~40 km (Fig. 1B).

73  
74 Figure 2 shows the interpreted seismic time sections along the two profiles that cross the rift  
75 valley; un-interpreted images are shown in Figure S1. Although the profiles are N-S, 25° NE off  
76 the orthogonal to the spreading axis, symmetry of structures on either side of the axial graben are  
77 clear, and show as well as the thick sediments filling the axial valley, and numerous faults  
78 penetrating down 2-2.5 s. The 7.5 s deep reflection is the Moho which appears intermittently  
79 along both profiles.

80  
81 In the absence of seismic refraction studies, we converted RMS velocities into interval velocities,  
82 laterally smoothed to obtain a continuous velocity and seismic image. Although the RMS-  
83 derived interval velocities are less accurate than those from refraction data, they provide insight  
84 into crustal structure. The P-wave velocity increases from 1.6 km/s near the seafloor to 3.0 km/s  
85 at the sedimentary sequence bottom/base? (Fig. S2), which combined with the linear seismic  
86 reflections suggest the presence of sedimentation layering. The alternating highly reflective and  
87 transparent layers within the sedimentary column could correspond to sediment deposits  
88 recording climate variability (Kluesner et al., 2014). Further below velocity increases sharply to  
89 4.5 km/s within a 0.6 s thick zone, associated with a layer displaying numerous bright  
90 reflections. Deeper and up to Moho, the reflective features are sparse but mostly steeply dipping.  
91 Lacking seismic reflectors, the seismic velocity in this region is poorly constrained.

92

## 93 **INTERPRETATION OF SEISMIC REFLECTORS AND RESULTS**

94

95 In this section we first focus our interpretation on the interaction between magma sills  
96 emplacement sedimentation, and the subsequent effects of faulting. We then address the nature of  
97 the crust-mantle boundary, to provide constraints on crustal accretion process at sedimented ridges.

98

### 99 **Low velocity reflectors**

100 Most of the reflections in the seismic profiles are of normal polarity as that of the seafloor  
101 reflection. However, both profiles display some reflections with reverse polarities (Figs.2A, 2B,  
102 2C, 2D),, which suggest low velocity zones likely induced by fluids or by material with lower  
103 velocity than that of the surrounding medium.

104 On-axis we observe two low velocity, reverse polarity reflectors. We suggest correspond to a  
105 magma bearing axial melt lens (AML), rather than other fluids such as water, as they are located  
106 below the ASSC axis; such reverse polarity reflections are commonly interpreted as the present  
107 of AMLs beneath fast spreading ridges (Detrick et al., 1987; Kent et al., 1993) and more recently  
108 at slow-spreading (Singh et al., 2006b) ridges. The shallowest one, which is 0.8 km wide at 6 s  
109 two-way travel time (TWTT) present on both profiles and we name it upper axial melt lens (U-  
110 AML). The second deeper one, which is 2-km wide at 7.2 s, is present only on profile PGS08-23  
111 and we name it lower axial melt lens (L-AML).

112 We also observe some reverse polarity reflections off-axis, but owing to their position and  
113 relatively short lateral extension, they probably correspond to fluids other than magma such as  
114 water or gas circulating near faults or along sediment-sill interfaces (Fig. 2).

115

116 **High velocity reflectors**

117 Within the sedimentary layers and underneath them, we observe two sets of strong and  
118 discontinuous normal polarity reflections (Figs. 2A, 2B) that should correspond to high, positive  
119 velocity contrasts. We interpret those that are sub-horizontal (sloping  $< 20^\circ$ ) as frozen igneous  
120 bodies or sills (Figs. 2A, 2B), following similar criteria used in other studies in similar  
121 environments (Trude et al. 2003; Lizarralde et al., 2011). These reflectors tilt primarily toward  
122 the axis, where they can show a saucer-shape (Hansen and Cartwright, 2006).  
123 Steeper reflections ( $>20^\circ$ ) can be interpreted either as highly rotated sills or as fault reflectors  
124 owing to their orientation and position in the proximity of prominent and continuous faults (Figs.  
125 2A, 2B). We prefer to interpret them as sills because, in the sedimentary strata, faults offset  
126 sediment layers and lack any reflectivity contrast (see below). Furthermore, the high reflectivity  
127 of the frozen magma sills below the sedimentary sequence requires a surrounding medium that is  
128 not of magmatic origin.

129

130 **Tectonic structures**

131 The 600 m deep and 12-km wide axial graben is flanked by a series of high-angle ( $65-75^\circ$ )  
132 normal faults. They have a  $\sim 1$  km spacing (Figs. 2A, 2B, 3A) with a staircase pattern, dipping  
133 towards the center of the basin, and are responsible for the local subsidence. These faults are  
134 recent as they cut through the most recent sediments. The seismic profiles and the seafloor  
135 bathymetry suggest that the nature of the graben deformation and associated faulting is similar  
136 along the whole segment.

137 Further away from the axis and central graben, shallow-dipping (20-40°) reflections at both  
138 flanks of the median valley are shown in PGS08-21, and only on one flank for PGS08-23. In  
139 some cases, these low-angle reflectors reach deep crustal levels and show a clear tilt of the  
140 adjacent crust block. This indeed suggests a fault-related flexural rotation resulting in a shallow  
141 dip of sedimentary reflectors away from the axis. This is best shown by two of the major inward-  
142 dipping low angle Outer Bounding Fault North and South faults (OBF-N and OBF-S in Figs. 2A,  
143 2B).

144 A clear bounding fault buried under more recent sediments is imaged around CMP 26000-27000  
145 (Fig. 2A). This fault penetrates down to 700 ms above the Moho, with 500 ms thick reflective  
146 zone above the fault's lower extent (Fig. 3B). A similar, but smaller, structure is present on the  
147 conjugate side to the south. On PGS08-23, these OBFs are also visible, and have some high  
148 angle faults in a staircase pattern below them. These low-angle reflections may thus be akin to  
149 the present-day seafloor surface of the axial graben flank. The identification of high-angle,  
150 staircase patterns is increasingly difficult nearing the transform fault in the east near profile  
151 PGS08-21, where the block rotation and the deformation are the highest. Locally, we observe a  
152 sediment infill that has been tilted away from the axis, consistent with flexural rotation  
153 associated with ridgeward normal faulting. Deep-rooted low-angle faults close to the axis rupture  
154 at the seafloor. Other faults are sealed by recent sediments, forming an unconformity with the  
155 tilted blocks. Hence, the faults responsible for the tilt of these blocks are not active at the present  
156 time. This observation, together with the lack of a tectonic signal on the most recent sediment  
157 cover, lack of fault scarpers at the seafloor away from the axis, and the concentration of seismicity  
158 along the axial graben (Diehl et al., 2013), clearly demonstrate that tectonic deformation  
159 concentrates along the graben. Little or no deformation occurs off-axis, and all the tectonic

160 structures observed off-axis have been passively rafted due to oceanic accretion on-axis, where  
161 we focus our analysis.

162

### 163 **Crust-Mantle boundary**

164 The Moho reflection is generally 1-5-2.5 s into the oceanic crust (Kent et al, 1994). On our data

165 it is imaged at ~7.6 s on profile PGS08-21 and around 7.5-7.8 s on profile PGS08-23. It is

166 slightly shallower beneath the axial valley (Figs. 2A, 2B), and can be followed along a

167 significant part of the profile. If the base of the sedimentary strata is the top of the oceanic crust

168 and the Moho reflection its base, then crustal thickness would vary from 1.6 s to 2.4 s. On Profile

169 PGS08-23, between CMP 77000 and 79000, the Moho displays a complex pattern, with lens-

170 type structures (Figs. 2B, 3C); similar reflectors are observed near CMP 16000 and 25000 on

171 profile PGS08-21, and around CMP 69000 and 80000 on profile PGS08-23. Beneath the

172 spreading axis we observed a weak reflection ~ 250 ms below the L-AML, which we also

173 interpret as the Moho.

174

## 175 **DISCUSSION AND CONCLUSIONS**

176

177 A combination of the interval P-wave velocity data and seismic reflection images of the full

178 crustal thickness allows us to characterize for the first time with sufficient detail the nature of the

179 whole crust formed along the axis of a sedimented spreading center.

180

### 181 **Axial melt supply**

182 Multiple melt lenses have been recently reported beneath fast spreading centers (Arnulf et al.,  
183 2014; Marjanovic et al., 2014), but the presence of two melt sills (U-AML and L-AML) beneath  
184 a slow spreading ridge is novel as it has been difficult to image melt lens below them (Singh et  
185 al., 2006b). Furthermore, the separation between the two melt sills is much larger ( $\sim 1.2$  s) than  
186 that observed at fast spreading ridge (0.2-0.3 s), and therefore, their roles should be different.  
187 The U-AML is relatively shallow when compared to the predicted depth for AMLs for the  
188 spreading rate of 3.8 cm/yr (Chen and Morgan 1990). In the absence of any enhanced melt  
189 supply to the axis, this prediction would suggest that the apparently shallow U-AML is likely a  
190 transient feature at this spreading rate, but instead the presence of the reflector on the two  
191 profiles 40-km apart indicates that the U-AML is instead a prevalent feature. This shallow melt  
192 lens position could also be facilitated by the thick sediment layer blanketing the axial valley,  
193 that likely acts as an insulating layer resulting a warmer thermal regime that could help retain a  
194 melt for longer time.

195 The U-AML, which lies at the base of the sedimentary cover, is also at the intersection of the  
196 median valley bounding faults, suggesting that the shallow dipping bounding faults may root at  
197 the U-AML. The U-AML is also shifted  $\sim 0.5$  km northward from the axial graben on PGS08-21  
198 and  $\sim 1.2$  km on PGS08-23, inducing the southern boundary fault to dip more shallowly than the  
199 northern one. Such an asymmetry in faulting caused by the AML position has also been  
200 suggested at the Afar rift (Grandin et al., 2009).

201 The depth of the L-AML, at  $\sim 2.3$  s below the seafloor or  $\sim 4.5$  km within the igneous crust, is  
202 consistent with the prediction from lithospheric cooling models at this spreading rate (Chen and  
203 Morgan, 1990). The L-AML likely feeds the U-AML on axis, and this magmatic system may be

204 the source for other crustal melt sills near and off the spreading axis now frozen, although the the  
205 dynamics and interactions of multiple melt lenses are not well-known.

206

### 207 **Formation of the upper crust**

208 We identify a steep gradient in P-wave velocity ranging from 3.0 to 4.5 km/s at the base of the  
209 recent sediments, clearly associated with the numerous sills observed at this depth (Fig. S2). As  
210 for the Guyamas basin (Kluesner et al., 2014), the reflectors in this area show amplitude  
211 whitening between sills, which could be due to fluid-expulsion and metamorphism or the  
212 presence of gas (steam). The P-wave velocity in the sediments is likely to increase due to  
213 compaction and fluid expulsion, and to metamorphism around sill intrusions (Aarnes et al.,  
214 2011). Based on the P-wave velocity, we suggest that the upper crust is a 1.2 km thick velocity  
215 gradient zone composed of metamorphosed sediments and sill intrusions (Fig. 4).

216 Deflation due to melt extraction in the U-AML, in addition to normal faulting along the axial  
217 graben, can contribute to axial subsidence and promote the inward tilt of the sill/sediment  
218 sequences. Extension concentrated at the rift valley and its flanks would thus induce the  
219 development of steeply dipping faults (stair-case normal faults), possibly facilitating further  
220 injection of sills in the upper sedimentary strata. High-amplitude reflections below the high-  
221 velocity gradient zone are sparse, sometimes concentrating as lenses along low-angle faults. The  
222 relatively higher velocity in this crustal section is indicative of magmatic accretion, but lacking  
223 adequate velocity constraints we do not exclude it to be metamorphosed sill-sediment lenses  
224 similar in composition to the upper crust. The former interpretation would be induced by the  
225 proximity of these faults with the magma supply at the axis. The latter one would suggest high  
226 variability of the metamorphic upper crustal thickness produced by locally high subsidence, and

227 is more consistent with the presence of high velocity contrasts required to image these  
228 reflections.

229 The U-AML can define the effective brittle-ductile boundary locally while it is active,  
230 controlling the location of the inner bounding faults. After a certain amount of extension and  
231 magmatism, a new inner bounding fault would develop inward from the existing bounding faults,  
232 the older faults becoming inactive, rafted off-axis, and buried by incoming sediments. With such  
233 a process, all sill-sediment sequence now present in the graben likely forms the bulk of the upper  
234 part of the oceanic crust here. These results also suggest that the magmatic crustal accretion at  
235 the ASSC is taken up solely by intrusive processes, consistent with the absence of clear magnetic  
236 anomalies that can be attributed to eruptive units (Kamesh Raju et al., 2004), and to the lack of  
237 volcanic features along the axial graben floor. Variation in magmatic supply to the AML could  
238 be responsible for the two modes of faulting of the ASSC and would exclude the hypothesis of a  
239 halt in the oceanic crustal accretion as suggested by Morley and Alvey, (2015). On the other  
240 hand, the L-AML may locally control the rheology of the lithosphere, pinnin the root of outer  
241 bounding fault, while the two melt lenses regulate activity on the outer and inner bounding  
242 faults, and hence the nature of the median valley (Fig. 4).

243

#### 244 **Crustal thickness and Moho transition**

245 Widespread Moho reflections allows us to constrain the nature of the lower crust and its base.  
246 Lacking accurate seismic refraction velocities, we assume a P-wave velocity of 6.8 km/s in the  
247 lower crust (e.g., Lizarralde et al., 2007). This yields a lower crustal thickness of <5.5 km, and a  
248 total crustal thickness of <6.7 km, overlain by 1.5 km of sediments, consistent with gravity-  
249 derived estimations.(Morley and Alvey (2015).

250 A complex Moho with lenses just above it could result from either dunite lenses (melt residue) or  
251 gabbro lenses in the mantle-crust transition zone. Frozen melt sills below the Moho have been  
252 observed beneath the Juan De Fuca Ridge (Nedimovic et al., 2005), but ASSC lenses seem to lie  
253 within the Moho transition zone, and could be the residue of former L-AMLs. The complex  
254 Moho transition zone with dunite-gabbro lenses observed in the Oman ophiolite (Braun and  
255 Kelemen, 2002) may be a suitable analog to the complex Moho we image here. The proximity of  
256 the Moho with lower melt lens creates a complex mantle transition zone, which combined with  
257 the presence of multiple sills, makes the sedimented ridge a special class of ocean spreading  
258 center forming unique marginal crust, but accurate seismic velocities are required to estimate the  
259 magmatic supply to the axis from the relative proportion of sediment and magma and its  
260 variation in depth.

261

## 262 **ACKNOWLEDGMENTS**

263

264 We would like to thank Petroleum Geo-Services (PGS) for providing the data, and Adrien Arnulf  
265 and Wayne Crawford for discussions.

266

## 267 **REFERENCES CITED**

268 Aarnes, I., Fristad, K., Planke, S., and Svensen, H., 2011, The impact of host-rock composition  
269 on devolatilization of sedimentary rocks during contact metamorphism around mafic sheet  
270 intrusions: *Geochemistry, Geophysics, Geosystems*, v. 12, no. 10, Q10019,  
271 doi:10.1029/2011GC003636.

272 Arnulf, A. F., Singh S. C., and Pye J. W., 2014, Seismic evidence of a complex multi-lens melt  
273 reservoir beneath the 9° N Overlapping Spreading Center at the East Pacific Rise:  
274 Geophysical Research Letters, v. 41, p. 6109-6115.

275 Braun, M. G., and Kelemen, P.B., 2002, Dunite distribution in the Oman ophiolite: Implications  
276 for melt flux through porous dunite conduits: Geochemistry, Geophysics, Geosystems, v. 3,  
277 no. 11, Q8603, DOI: 10.1029/2001GC000289.

278 Buck, W. R., Lavier, L. L., and Poliakov, A. N. B., 2005, Modes of faulting at mid-ocean ridges:  
279 Nature, v. 434, p. 719-723.

280 Bruvoll, V., Breivik, A. J., Mjelde, R., and Pedersen, R., B., 2009, Burial of the Mohn-  
281 Knipovich seafloor spreading ridge by the Bear Island Fan: Time constraints on tectonic  
282 evolution from seismic stratigraphy: Tectonics, v. 28, no. TC4001, DOI:  
283 10.1029/2008TC002396.

284 Chen, Y., and Morgan, W. J., 1990, A Nonlinear Rheology Model for Mid-Ocean Ridge Axis  
285 Topography: Journal of Geophysical Research, v. 95, p. 17583-17604.

286 Curray, J. R., Moore, D. G., Lawver, L. A., Emmel, F. J., Raitt. R. W., Henry, M., and  
287 Kieckhefer, R., 1979, Tectonics of Andaman Sea and Burma, *in* J. S. Watkins, L.  
288 Montadert and P. W. Dickerson, eds, Geological and Geophysical Investigations of  
289 Continental Margins edited by: American Association Petrology Geology, Memoir 29,  
290 p. 189–198.

291 Davis, E.E., and Becker, K., 2002, Observations of natural-state fluid pressures and temperatures  
292 in young oceanic crust and inferences regarding hydrothermal circulation: Earth and  
293 Planetary Science Letters, v. 204, p. 231-248.

294 Detrick, R. S, Buhl, P., Vera, E., Mutter, J., Orcutt, J., Madsen, J., and Brocher, T., 1987, Multi-

295 channel seismic imaging of a crustal magma chamber along the East Pacific Rise: *Nature*, v.  
296 326, p. 35-41.

297 Diehl, T., Waldhauser, F., Cochran, J. R., Kamesh Raju, K. A., Seeber, L., Schaff, D., and  
298 Engdahl, 2013, Back-arc extension in the Andaman Sea: Tectonic and magmatic processes  
299 imaged by high-precision teleseismic double-difference earthquake relocation: *Journal of*  
300 *Geophysical Research: Solid Earth*, v. 118, p. 1-19.

301 Fitch, T. J., 1972, Plate convergence, Transcurrent Faults, and Internal Deformation  
302 Adjacent to Southeast Asia and the Western Pacific: *Journal of Geophysical Research*,  
303 v. 77, p. 4432-4460.

304 Grandin, R., et al., 2009, September 2005 Manda Hararo-Dabbahu rifting event Afar  
305 (Ethiopia) : Constraints provided by geodetic data : *Journal of Geophysical Research*,  
306 v. 114, no. B08404, DOI: 10.1029/2008JB005843.

307 Hansen, D., M., and Cartwright, J., 2006, The three-dimensional geometry and growth of  
308 forced folds above saucer-shaped igneous sills: *Journal of Structural Geology*, v. 28, p.  
309 1520-1535.

310 Kamesh Raju, K. A., Ramprasad, T., Rao, P. S., Ramalingeswara Rao, B., and Varghese, J.,  
311 2004, New insights into the tectonic evolution of the Andaman basin, northeast Indian  
312 Ocean: *Earth and Planetary Science Letters*, v. 221, p. 145-162.

313 Kent, G. M., Harding, A. J., Orcutt, J. A., 1993, Distribution of Magma Beneath the East Pacific  
314 Rise Between the Clipperton Transform and the 9°17'N Deval From Forward Modeling of  
315 Common Depth Point Data: *Journal of Geophysical Research*, v. 98, p. 13945-13969.

316 Kent, G. M., Harding, A. J., Orcutt, J. A., Detrick, R. S., Mutter, J. C., Buhl, P., 1994, Uniform  
317 accretion of oceanic-crust south of the Garrett transform at 14-degrees-15's on the East

318 Pacific Rise: Journal of Geophysical Research-Solid Earth, v. 99, p. 9097-9116.

319 Kluesner, J., Lonsdale, P., and González-Fernández, A., 2014, Late Pleistocene cyclicity of  
320 sedimentation and spreading-center structure in the Central Gulf of California: Marine  
321 Geology, v. 347, p. 58-68.

322 Lizarralde, D., et al., 2007, Variation in styles of rifting in the Gulf of California: Nature, v. 448,  
323 p. 466-469.

324 Lizarralde, D., Adam Soule, S., Seewald, J. S., Proskurowski, G., 2011, Carbon release by off-  
325 axis magmatism in a young sedimented spreading centre: Nature Geoscience, v. 4, p. 50–54.

326 Marjanović, M., Carbotte, S. M., Carton, H., Nedimović, M. R., Mutter J. C., and Canales, J. P.,  
327 2014, A multi-sill magma plumbing system beneath the axis of the East Pacific Rise: Nature  
328 Geoscience, v. 7, p. 825-829.

329 Morley, C.K., and Alvey, A., 2015, Is spreading prolonged, episodic or incipient in the Andaman  
330 Sea? Evidence from deepwater sedimentation: Journal of Asian Earth Sciences, v. 98, p.  
331 446-456.

332 Nedimović, M. R., Carbotte, S. M., Harding, A. J., Detrick, R. S., Pablo Canales, J., Diebold, J.  
333 B., Kent, G. M., Tischer, M., and Babcock, M. J., 2005, Frozen magma lenses below the  
334 oceanic crust: Nature, v. 436, p. 1149-1152.

335 Needham, H. D., and Francheteau, J., 1974, Some characteristics of the rift valley in the Atlantic  
336 ocean near 36°48' North: Earth and Planetary Science Letters, v. 22, p. 29–43.

337 Sieh, K., and Natawidjaja, D., 2000, Neotectonics of the Sumatran fault, Indonesia: Journal of  
338 Geophysical Research, v. 105, p. 28295-28326.

339 Singh S. C., et al., 2006b, Discovery of a magma chamber and faults beneath a Mid-Atlantic

340 Ridge hydrothermal field: Nature, v. 442, p. 1029-1032.  
341 Smith, W. H. F., and Sandwell, D. T., 1997, Global sea floor topography from satellite altimetry  
342 and ship depth sounding: Science, v. 227, p. 1956-1962.  
343 Trude, J., Cartwright, J., Davies, R., J., and Smallwood, J., 2003, New technique for dating  
344 igneous sills: Geology, v. 31, no. 9, p. 813-816.

345

## 346 **FIGURE CAPTIONS**

347

348 Figure 1: **Andaman Sea Spreading Centre**: A: General map of the study area (Multibeam  
349 bathymetry from Kamesh Raju et al., 2004 added to the bathymetry of Smith and Sandwell,  
350 1997). ANF: Andaman Nicobar Fault, SFS: Sumatra Fault System. Red line: Andaman Sea  
351 Spreading Centre (ASSC). ATF: Andaman Transform Fault. Black box indicates area shown in  
352 Figure 1b. Arrows indicate the sense of the movement. B: Detailed map of the Andaman Sea  
353 spreading center. Black lines indicate normal faults. The red lines indicate the seismic lines  
354 shown in this study.

355

356 Figure 2: **Seismic profiles**: Interpreted seismic images A: PGS08-21 and B: PGS08-23. Time  
357 here is a two-way travel time. The black dashed box refers to Figure 3A. The black boxes mark  
358 the images shown in Figures 3B and 3C. CMP: Common Mid-Point. Blue horizons indicate the  
359 seafloor. Active faults are indicated by black lines and inactive by dashed black lines. Sills are  
360 highlighted by orange lines, possible hydrothermal deposits by dark blue lines, possible fluids by  
361 light blue lines and the Moho by pink lines. The dashed pink lines indicate the top of the  
362 reflective zone above the Moho. Green lines highlight some horizons in the sediments, variations

363 in the green color is made to differentiate the sedimentary units. Red lines mark melt lenses. U-  
364 AML: Upper Axial Melt Lens and L-AML: Lower Axial Melt Lens. The dark boxes mark the  
365 images shown in C and D. C: Seafloor fattened image beneath valley floor for profile PGS08-21.  
366 Small black boxes indicate polarity plots, from top to bottom: Polarity of the seafloor, polarity of  
367 a sill, and polarity of the U-AML. D: Seismic image with L-AML flatten. Small black boxes  
368 indicate polarity plots, from top to bottom: polarity of a sill near the seafloor, complex area with  
369 no clear polarity, polarity of the U-AML, polarity of the L-AML.

370

371 **Figure 3: Expanded view of seismic data:** Interpretation uses the same colors as figure 2. A:  
372 Depth converted seismic image in the median valley along profile PGS08-21. The velocity  
373 model used is the one in supplementary Figure S2. The thickness of the faults is proportional to  
374 the offset they induce. B: Time (not depth converted) blow-up of seismic image of a buried  
375 bounding fault and associated sills, C: Time (not depth converted) blow-up of a reflective zone  
376 above the Moho.

377

378 **Figure 4: Crustal model of sedimented ASSC:** Schematic 3D block diagram synthesizing  
379 different features observed along both profiles. The block diagram differentiates un-  
380 metamorphosed sedimentary layers in green, yellow and white, upper crust in light brown, lower  
381 crust in brown, mantle transition zone in purple and mantle in pink. The blue line shows the  
382 position of the 1.5, 3.0 and 4.5 km/s velocity limit (from figure S2). On the right, a diagram  
383 proposes the respective proportions of the sediments versus the igneous material.

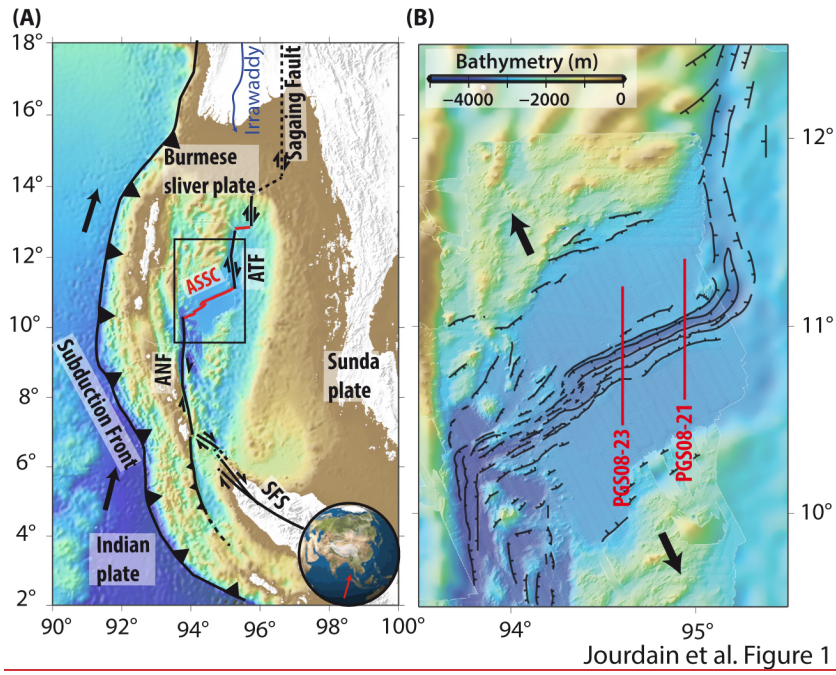
384

385 **Figure S1: Un-interpreted seismic images:** A: Profile PGS08-21. B: Profile PGS08-23.

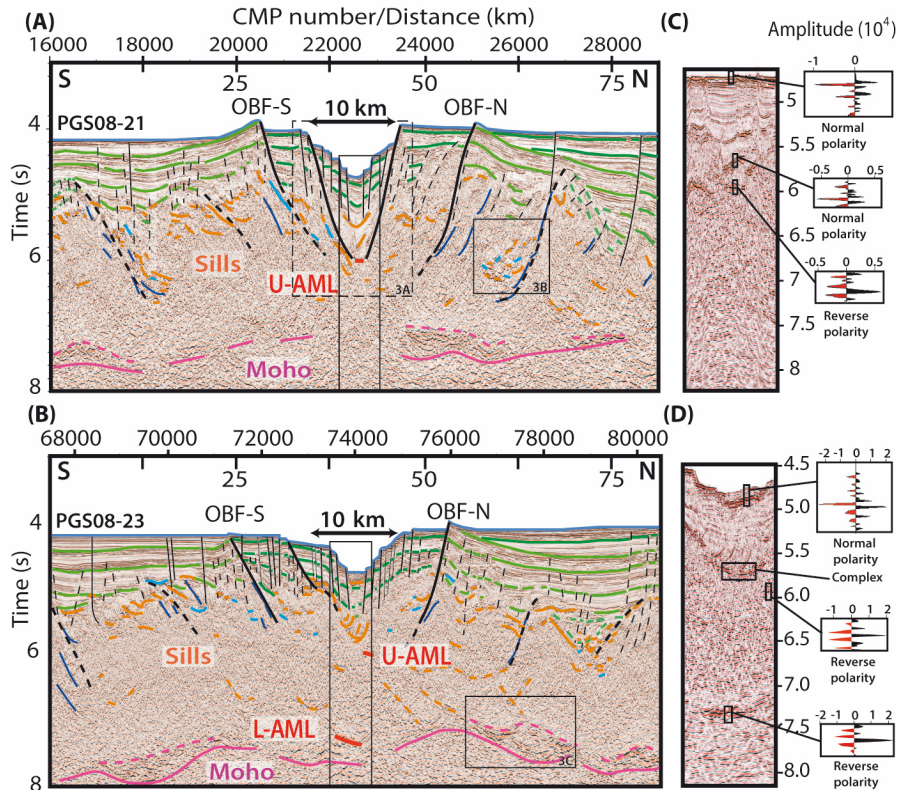
386

387 Figure S2: **Interval Velocity:** Interval velocity as a function of time derived from the root mean

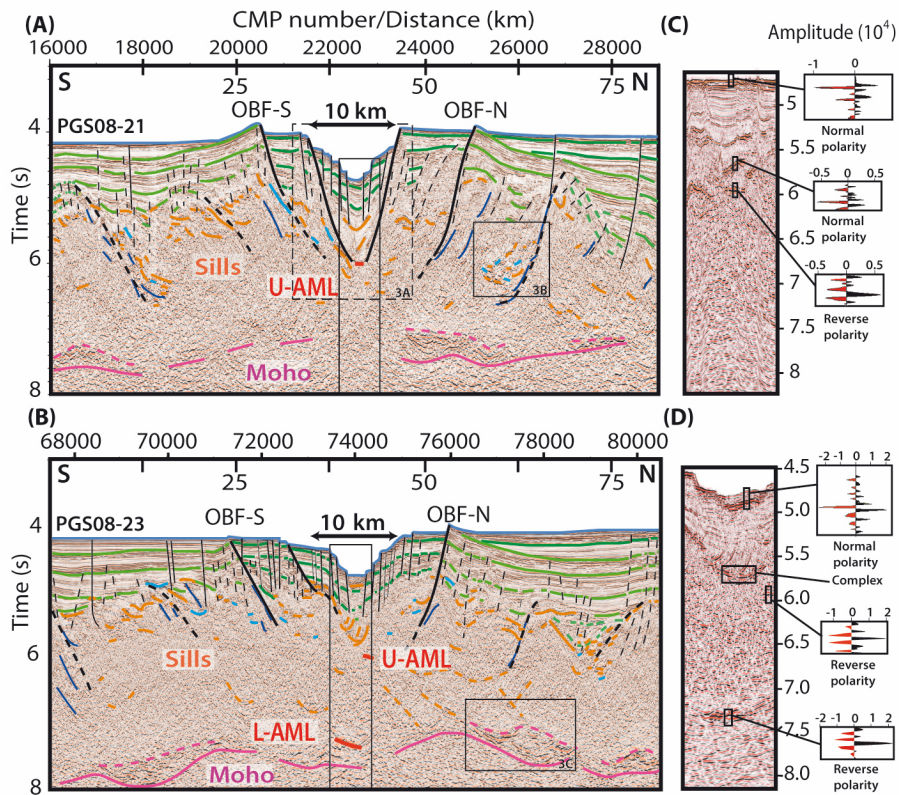
388 square velocity superimposed on the interpreted profile PGS08-21 (Fig. 2A).



389



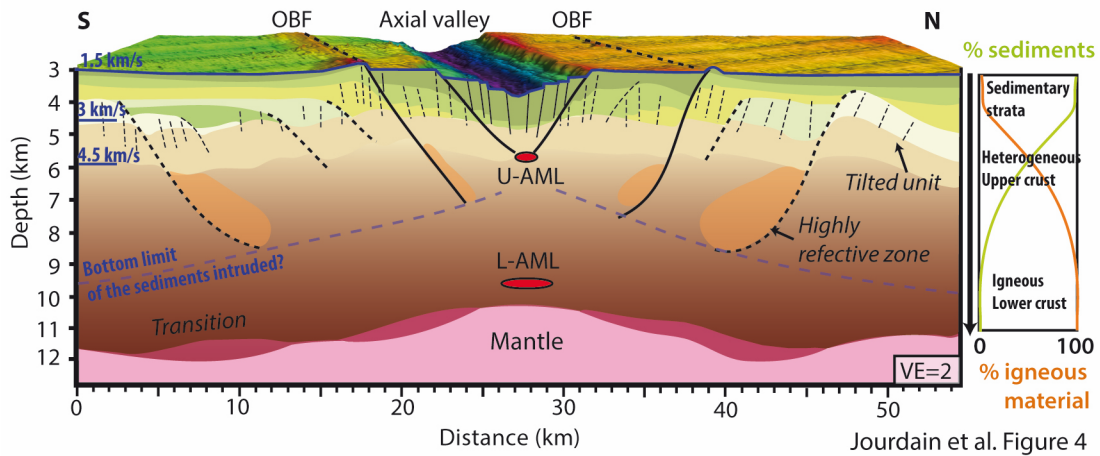
Jourdain et al. Figure 2



Jourdain et al. Figure 2

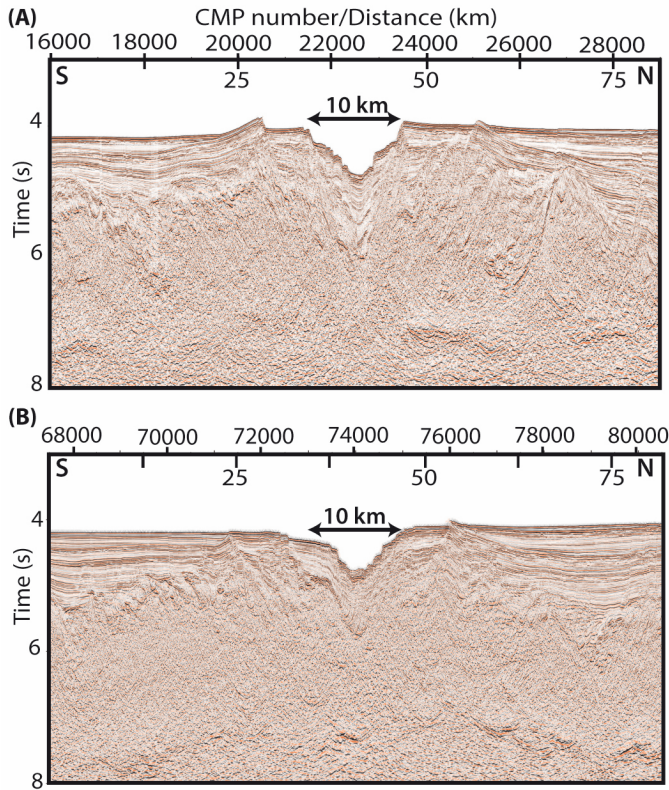
390

391



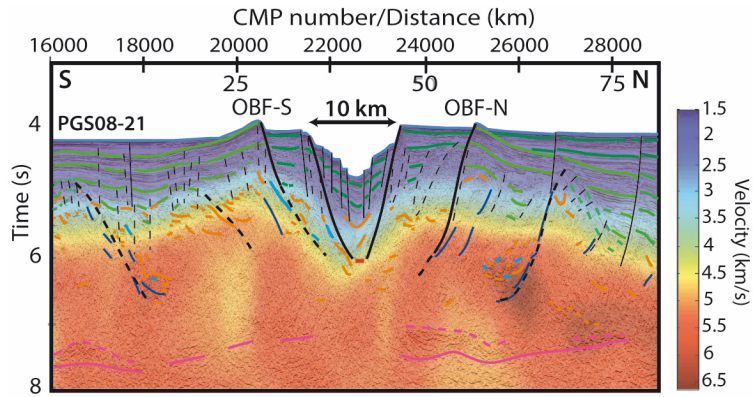
Jourdain et al. Figure 4

392



Jourdain et al. Figure S1

393



394

Jourdain et al. Figure S2